Computational anatomy and geometric shape analysis enables analysis of complex craniofacial phenotypes in zebrafish mutants

Kelly M. Diamond[1], Sara M. Rolfe[1,2], Ronald Y. Kwon[3,4], A. Murat Maga[1,5]

[1] Center for Developmental Biology and Regenerative Medicine, Seattle Children's Research Institute, Seattle, WA, USA

[2] Friday Harbor Marine Laboratories, University of Washington, San Juan, WA, USA

[3]Department of Orthopedics and Sports Medicine, University of Washington, Seattle, WA, USA

[4]Institute for Stem Cell and Regenerative Medicine, University of Washington, Seattle, WA, USA

[5]Division of Craniofacial Medicine, Department of Pediatrics, University of Washington, Seattle, WA, USA

Abstract

Computational anatomy (CA) approaches start by estimating a canonical 'template' from a sample of images. This template is then used as a basis for statistical analysis to quantify structural differences among groups of interest. Due to the complexity of fish skulls, previous attempts to classify craniofacial phenotypes have relied on qualitative features or 2D landmarks. In this work we aim to identify and quantify differences in 3D craniofacial phenotypes in adult zebrafish mutants. We first estimate a synthetic 'normative' zebrafish template using microCT scans from a sample pool of wildtype animals using the Advanced Normalization Tools (ANTs). To validate the accuracy of the template and our CA pipeline, we compared the otolith volumes derived from the CA approach to manually segmented volumes of the same set of zebrafish. Our overall CA based segmentation volumes are statistically similar to our manual segmentations and both results show that mutants have larger otoliths than their wildtype controls. We apply CA to zebrafish with somatic mutations in *bmp1a*, whose human ortholog when disrupted is associated with Osteogenesis Imperfecta. Our Generalized Procrustes Analysis separated the bmp1a and wildtype fish along the first two principal components which collectively explained 31.8% of the variation in the dataset. Compared to controls, the phenotypic differences in *bmp1a* fish are concentrated around the operculum and the orbit. Our CA approach seems to offer a potential pipeline for high throughput screening of complex fish craniofacial phenotypes, especially those of zebrafish which are an important model system for testing genome to phenome relationships in the study of development, evolution, and human diseases.

Key words: cranial morphology, osteogenesis imperfecta, geometric morphometrics, computational anatomy

Introduction

The two main drivers of an organism's phenotype are the underlying genetic makeup and the environment in which an organism is exposed during development. Current best practices for quantifying the relationship between genotype and phenotype is to compare the phenotype of known genetic mutants to their wildtype siblings under identical rearing conditions (Houle et al., 2010; Watson et al., 2020). These methods minimize the environmental effect, allowing for differences among groups to be associated with a specific genetic mutation. One area where these methods are being actively developed is with zebrafish and other laboratory fish models with mutations in genes whose human orthologs when disrupted cause skeletal diseases (Busse et al., 2019; Kwon et al., 2019; Watson et al., 2020).

Osteogenesis Imperfecta (OI) is a disease of the collagen matrix and results in brittle bones and skeletal deformities (Busse et al., 2019). Different forms of OI are caused by mutations in genes that encode for components of the collagen matrix and associated proteins. One such gene is Bone Morphogenetic Protein 1 (*BMP1*), which encodes for a secreted protein involved in procollagen processing. Individuals with mutations in *BMP1* exhibit increased bone mineral density and recurrent fractures (Asharani et al., 2012). In zebrafish, an ortholog of *BMP1* is *bmp1a*, which shows conserved function in osteogenesis across species and is required for mature collagen generation downstream of osteoblast maturation in bone (Asharani et al., 2012). *bmp1a* mutants exhibit ectopic accumulation of minerals in bone, causing malformation

66 and fractures in adult skeletal structures (Asharani et al., 2012). Severe forms of OI are
67 frequently associated with craniofacial abnormalities (Dagdeviren et al., 2019). Previous work in
68 *bmp1a* zebrafish mutants have identified phenotypic patterns across the axial skeleton that
69 distinguish *bmp1a* mutants from wildtype siblings (Hur et al., 2017). However, due to the
70 complicated structure of the fish cranial skeleton, craniofacial abnormalities in zebrafish OI
71 models have mostly focused on qualitative phenotypes (Gistelinck et al., 2018), and little work
72 has been done to quantify complex cranial phenotype.
73 The traditional methods for quantifying cranial morphology use homologous landmark points
74 on 2D images of the lateral view of the head (Sidlauskas, 2008). However, the requirement for
75 homologous structures limits landmark placement across the skull, and hence may miss the
76 phenotypic variation in these areas. Here we propose using an atlas-based computational
77 anatomy (CA) approach to build a template and then using a pseudo-landmark pipeline to
78 identify areas of the skull that vary among mutant and wildtype fish. Atlas-based approaches
79 estimate an unbiased anatomical 'template' from a group of images (Guimond et al., 2006), and
80 then use this template to the basis to assess shape differences among groups of interest
81 (Ashburner and Friston, 2000). Atlas-based approaches have been used to characterize
82 phenotypes in many neuroimaging studies in humans, in fetal mice (KOMP2 project) as well as
83 in the mouse cranial skeleton (Maga et al., 2017; Toussaint et al., 2020). We define pseudo-
84 landmarks here as landmarks that are not homologous but evenly cover the surface of our fish
85 skulls. These methods aim to quantify the cranial phenotype associated with mutations in
86 zebrafish with minimal user intervention so that large scale studies can examine phenotype-
87 genotype associations in the skeletal system can be accomplished in a high-throughput fashion.

88 **Methods**

89 Zebrafish microCT scans used in this study were acquired as part of a previous study, for full
90 animal use information involved in that study see Watson et al., 2020. We used a total of 23
91 wildtype fish from two clutches ("wildtype fish") to build our atlas and used 12 *bmp1a* somatic
92 mutants ("*bmp1a* fish"), from a single clutch. Somatic *bmp1a* mutants are mosaic for mutations
93 in *bmp1a*. Watson et al., 2020 performed a comparison of *bmp1a* somatic and germline
94 mutants and showed that somatic *bmp1a* mutants recapitulate germline *bmp1a* mutant
95 phenotypes, but possess additional phenotypic variability due to mosaicism. We focused our
96 analyses on *bmp1a* somatic mutants as they provide a real-world sample of phenotypic
97 variability likely to be encountered in CRISPR-based reverse genetic screens (Shah et al., 2015;
98 Watson et al., 2020).

99 *MicroCT Imaging and Atlas Building*

100 Imaging was performed using a vivaCT40 (Scanco Medical, Switzerland) at 21 micron voxel
101 resolution (55kVp, 145mA, 1024 samples, 500proj/180˚, 200 ms integration time). Files of
102 individual fish were reconstructed using Scanco software to create 3D volume files for each fish
103 in the study. To investigate potential asymmetry patterns, we opted to build a symmetrical
104 atlas of wildtype fish (N=23) by first reflecting all volumes along the sagittal plane. A symmetric
105 atlas was generated using the antsMultivariateTemplateConstruction2.sh script as provided by
106 the Advance Normalization Tools (Avants et al., 2014), using the default settings. Atlas building
107 script initiates with a linear average of all samples, to which all samples are deformable
108 registered to (Figure 1). The resultant deformation fields are applied to samples, and a new

109 average is estimated and then used as a new reference for the next step of registrations. Four
110 iterations were sufficient to obtain a symmetrical and anatomically detailed template.

111 *Atlas validation*

112 First, we review the resultant atlas qualitatively by investigating the spatial arrangement of
113 bones in 3D rendering. To quantitatively validate the atlas and our computational anatomy
114 framework, we first created segmentations of individual otoliths from every sample manually
115 using the open-source 3D Slicer program (Fedorov et al., 2012). We chose otoliths because they
116 are dense, spread out along the dorsoventral axis of the crania, and do not touch any bones,
117 which minimized the potential for error in our manual segmentations that serve as the ground
118 truth data. The otoliths from the atlas are segmented in the same manner. Next, we
119 deformably register every sample, including the mutants, to our atlas using the ANTsR package,
120 and apply the resultant transformation field to our atlas otolith segmentation to map them
121 directly onto the subject space. From this mapping, we calculated the volumes of CA derived
122 segmentation and statistically compared them to ground truth. All statistical analysis and image
123 registrations are done using the R extensions of the ANTs ecosystem (Avants, 2020).

124 *Analysis of ZF cranial shape difference in wild-types and mutants.*

125 Because a standard set of cranial landmarks in fish skulls (Sidlauskas, 2008) are too sparse to
126 adequately represent the complex shape of fish skulls and to capture potential local shape
127 differences, we opted to use pseudo-landmarks. Pseudo-landmarks are geometrically
128 constructed points. SlicerMorph's PseudoLMGenerator provides a convenient interface to
129 estimate a dense point-cloud from a mesh, using its geometry (Rolfe et al., 2021; Figure 1). For
130 bilaterally symmetric structures, PseudoLMGenerator allows users to define the axis of

131 symmetry around which pseudo-landmarks are symmetrically reflected, allowing for
132 asymmetry analyses. More implementation and technical specifics regarding
133 PseudoLMGenerator can be found in the cited paper above.

134 We have segmented the skull as a single structure from our atlas, as well as individual
135 samples using the Segment Editor module in 3D Slicer by exporting the segment as 3D surface
136 model. We used the Surface Toolbox module in 3D slicer to decimate the model to create a
137 smoother surface mesh with more uniform vertex distribution. The 3D skull model from our
138 symmetric atlas was input into PseudoLMGenerator. Using the original mesh geometry and the
139 sagittal plane as the axis of symmetry, we generated a dense point cloud. One author (KMD)
140 then went through the pseudo-landmarks and removed the points that were on both jaws and
141 gills using the SlicerMorph's MarkupEditor. Both of those structures are highly prone to plastic
142 post-mortem deformation due to handling and preservation, as such they represent confound
143 non-biological variation. The ALPACA module in SlicerMorph provides a convenient interface to
144 transfer points on a reference mesh (in this case the symmetric template) to new subjects using
145 linear and deformable mesh registration (Porto et al., 2020). We used the default settings and
146 skipped the scaling option to transfer pseudo-landmarks from the atlas to all meshes in our
147 sample (Figures 1,2).

148 *Analysis*

149 To explore differences between *bmp1a* and wildtype fish, we first ran a Generalized Procrustes
150 Analysis on the 372 pseudo-landmark points using the GPA module in SlicerMorph (Rolfe et al.,
151 2021). Procrustes ANOVA on principal components is used to assess the significance of PCA
152 results using the geomorph package in R (Adams and Otárola-Castillo, 2013). Visualizations

153 were performed in the GPA module of SlicerMorph and using ggplot in R (Wickham and Chang,
154 2007).
155
156 **Results & Discussion**
157 When analyzing otoliths, we did not find significant differences between manually segmented
158 volumes and atlas segmented volumes (t=-0.912, p=0.363; Figure 3), though there were some
159 differences between some of the individual otoliths (Table 2; Figure 3). The most apparent
160 difference between *bmp1a* and wildtype fish is that *bmp1a* fish have larger otoliths than
161 wildtype fish, especially for the asteriscus, the largest otoliths in the zebrafish (Table 1; Figure
162 3). In contrast to bone formation in which the mineral phase is primarily hydroxyapatite,
163 otoliths are formed via an accumulation of calcium carbonate in the acellular endolymph of the
164 fish inner ear (Payan et al., 2004). Previous work found higher tissue mineral density in *bmp1a*
165 fish across the axial skeleton (Hur et al., 2017) and this result suggests potential influence of
166 *bmp1a* on other pathways associated with mineralized tissues.
167 Looking next at the results of our pseudo-landmark pipeline, we again find differences in
168 cranial phenotype between *bmp1a* and wildtype fish. We found significant differences between
169 *bmp1a* and wildtype fish for both PC1, which explained 22% of the variation in the data
170 (F=3.959; Z=1.316; p=0.036), and PC2, which explained 9.8% of the variation in the data
171 (F=4.528; Z=1.669; p=0.019; Figure 4). When we visualize the variation observed across our
172 pseudo-landmark points, we see higher instances of variation in the posterior portion of the
173 operculum, and around the orbit (longer vectors in Figure 5). As we removed pseudo-landmark
174 points associated with areas of the skull that varied due to preservation or scanning methods,

these represent areas of interest for exploring how phenotype differs between mutant and wildtype fishes. PC1 shows greater variation around the dorsal portion of the orbit and the right posterior operculum (green vectors in Figure 5). Whereas PC2 shows greater variation on the ventral portion of the orbit and left ventral opercula (dark blue vectors in Figure 5). Together these results provide evidence for phenotypic effects of the *bmp1a* mutation on the cranial phenotype of zebrafish. Future work should expand the number of families to ensure this is not unique to this particular family. We have shown how our pipeline can identify areas of greatest variation among groups of animals. In combination with additional morphological analyses, we hope this pipeline will enable researchers to better define the links between genotype and phenotype.

Acknowledgements

We thank members of the Maga and MSB labs for feedback and development of this project. This project was partly supported by National Science Foundation grants An Integrated Platform for Retrieval, Visualization and Analysis of 3D Morphology from Digital Biological Collections (DBI/1759883) and Biology Guided Neural Networks for discovering phenotypic traits (OAC/1939505) to AMM. RYK was supported by NIH Grant AR074417.

Competing Interests

The authors declare no competing interests

Author Contributions

Contribution of fish and microCT scans: RYK. Conceptualization and methodology: all authors, Writing: KMD; Editing and approval: all authors.

197 **Data availability**

198 Atlas and pseudo-landmark points are available at:

199 https://github.com/SlicerMorph/ZF_Skull_atlas/

200

201 **Literature Cited**

202 Adams, D.C., Otárola-Castillo, E., 2013. Geomorph: An r package for the collection and analysis

203 of geometric morphometric shape data. Methods Ecol. Evol. 4, 393–399.

204 Asharani, P. V., Keupp, K., Semler, O., Wang, W., Li, Y., Thiele, H., Yigit, G., Pohl, E., Becker, J.,

205 Frommolt, P., Sonntag, C., Altmüller, J., Zimmermann, K., Greenspan, D.S., Akarsu, N.A.,

206 Netzer, C., Schönau, E., Wirth, R., Hammerschmidt, M., Nürnberg, P., Wollnik, B., Carney,

207 T.J., 2012. Attenuated BMP1 function compromises osteogenesis, leading to bone fragility

208 in humans and Zebrafish. Am. J. Hum. Genet. 90, 661–674.

209 Ashburner, J., Friston, K.J., 2000. Voxel-based morphometry - The methods. Neuroimage 11,

210 805–821.

211 Avants, B.B., 2020. ANTsR: ANTs in R: Quantification tools for biomedical images version

212 0.5.7.5.

213 Avants, B.B., Tustison, N.J., Johnson, H., 2014. Advanced Normalization Tools (ANTs).

214 Busse, B., Galloway, J.L., Gray, R.S., Harris, M.P., Kwon, R.Y., 2019. Zebrafish: An Emerging

215 Model for Orthopedic Research. J. Orthop. Res.

216 Dagdeviren, D., Tamimi, F., Lee, B., Sutton, R., Rauch, F., Retrouvey, J.-M., 2019. Dental and

217 craniofacial characteristics caused by the p.Ser40Leu mutation in IFITM5. Am. J. Med.

218 Genet. 176, 65–70.

219 Fedorov, A., Beichel, R., Kalpathy-Cramer, J., Finet, J., JC, F.-R., Pujol, S., Bauer, C., Jennings, D.,
220 Fennessy, F., Sonka, M., Buatti, J., Aylward, S., Miller, J., Pieper, S., Kikinis, R., 2012. 3D
221 Slicer as an image computing platform for the quantitative Imaging Network. Magn Reson
222 Imaging 30, 1323–1241.
223 Gistelinck, C., Kwon, R.Y., Malfait, F., Symoens, S., Harris, M.P., Henke, K., Hawkins, M.B., Fisher,
224 S., Sips, P., Guillemyn, B., Bek, J.W., Vermassen, P., De Saffel, H., Witten, P.E., Weis, M.A.,
225 De Paepe, A., Eyre, D.R., Willaert, A., Coucke, P.J., 2018. Zebrafish type I collagen mutants
226 faithfully recapitulate human type I collagenopathies. Proc. Natl. Acad. Sci. U. S. A. 115,
227 E8037–E8046.
228 Guimond, A., Meunier, J., Thirion, J., 2006. Average Brain Models : A Convergence Study To cite
229 this version : Average Brain Models : A Convergence Study.
230 Houle, D., Govindaraju, D.R., Omholt, S., 2010. Phenomics: The next challenge. Nat. Rev. Genet.
231 11, 855–866.
232 Hur, M., Gistelinck, C.A., Huber, P., Lee, J., Thompson, M.H., Monstad-Rios, A.T., Watson, C.J.,
233 McMenamin, S.K., Willaert, A., Parichy, D.M., Coucke, P., Kwon, R.Y., 2017. MicroCT-Based
234 Phenomics in the Zebrafish Skeleton Reveals Virtues of Deep Phenotyping in a Distributed
235 Organ System. Elife 6, e26014.
236 Kwon, R.Y., Watson, C.J., Karasik, D., 2019. Using zebrafish to study skeletal genomics. Bone
237 126, 37–50.
238 Maga, A.M., Tustison, N.J., Avants, B.B., 2017. A population level atlas of Mus musculus
239 craniofacial skeleton and automated image-based shape analysis. J. Anat. 231, 433–443.
240 Payan, P., De Pontual, H., Bœuf, G., Mayer-Gostan, N., 2004. Endolymph chemistry and otolith

241 growth in fish. Comptes Rendus - Palevol 3, 535–547.
242 Porto, A., Rolfe, S.M., Maga, A.M., 2020. ALPACA: a fast and accurate approach for automated
243 landmarking of three-dimensional biological structures. bioRxiv.
244 Rolfe, S., Pieper, S., Porto, A., Diamond, K., Winchester, J., Shan, S., Kirveslahti, H., Boyer, D.,
245 Summers, A., Maga, A.M., 2021. SlicerMorph: An open and extensible platform to retrieve,
246 visualize and analyze 3D morphology. bioRxiv.
247 Shah, A.N., Davey, C.F., Whitebirch, A.C., Miller, A.C., Moens, C.B., 2015. Rapid reverse genetic
248 screening using CRISPR in zebrafish. Nat. Methods 12, 535–540.
249 Sidlauskas, B., 2008. Continuous and arrested morphological diversification in sister clades of
250 characiform fishes: A phylomorphospace approach. Evolution (N. Y). 62, 3135–3156.
251 Toussaint, N., Redhead, Y., Liu, W., Fisher, E.M.C., Hallgrimsson, B., Tybulewicz, V.L.J., Schnabel,
252 J.A., Green, J.B.A., 2020. Application of high-resolution landmark-free morphometrics to a
253 mouse model of Down Syndrome reveals a tightly localised cranial phenotype. BioRxiv.
254 Watson, C.J., Monstad-Rios, A.T., Bhimani, R.M., Gistelinck, C., Willaert, A., Coucke, P., Hsu,
255 Y.H., Kwon, R.Y., 2020. Phenomics-Based Quantification of CRISPR-Induced Mosaicism in
256 Zebrafish. Cell Syst. 10, 275-286.e5.
257 Wickham, H., Chang, W., 2007. ggplot2: An Implementation of the Grammar of Graphics. GNU
258 General Public License. https://cran.r-project.org/web/packages/ggplot2. Cran.
259
260
261
262

263 **Tables and Figures**

264 **Table 1.** Welch two sample t-test for difference between mutants and wildtype fish for each
265 pair of manually segmented otolith volumes. We provide the mean volumes(x) for mutants and
266 wildtype groups, degrees of freedom (df), test statistic (t), p value (p), and confidence interval
267 (UCL-LCL).

Otolith	**x mutant (mm^3)**	**x wildtype (mm^3)**	**df**	**t**	**p**	**UCL**	**LCL**
Left asteriscus	0.044	0.039	15.975	3.383	0.004	0.002	0.008
Right asteriscus	0.044	0.040	14.62	3.232	0.006	0.002	0.007
Left lapilus	0.026	0.025	18.013	2.000	0.061	-0.0007	0.003
Right lapilus	0.026	0.025	17.693	1.554	0.138	-0.0004	0.003
Left sagitta	0.005	0.005	18.665	2.244	0.037	0.0003	0.009
Right sagitta	0.005	0.005	15.375	1.902	0.076	-0.0005	0.008

268

269

270

271

272

273

274

275

276

277

278

279

Table 2. Welch two sample t-test for difference between manual and atlas-segmented otolith volumes for mutant and wildtype fish. We provide the mean volumes(x) for each method, degrees of freedom (df), test statistic (t), p value (p), and confidence interval (UCL-LCL).

Otolith	**group**	**x atlas (mm^3)**	**x manual (mm^3)**	**df**	**t**	**p**	**UCL**	**LCL**
Left asteriscus	mutant	0.042	0.044	21.971	-0.902	0.377	-0.006	0.044
Left asteriscus	wildtype	0.037	0.039	25.117	-1.998	0.057	-3.995	6.056
Right asteriscus	mutant	0.043	0.044	21.997	-0.618	0.543	-0.005	0.003
Right asteriscus	wildtype	0.037	0.040	20.891	-2.744	0.012	-0.005	-0.0007
Left lapilus	mutant	0.024	0.026	22.000	-3.074	0.006	-0.005	-0.0009
Left lapilus	wildtype	0.022	0.025	25.581	-5.438	<0.001	-0.004	-0.002
Right lapilus	mutant	0.023	0.026	20.94	-2.490	0.021	-0.005	-0.0005
Right lapilus	wildtype	0.021	0.025	24.294	-5.347	<0.001	-0.005	-0.002
Left sagitta	mutant	0.006	0.005	17.619	1.998	0.061	-0.00004	-0.002
Left sagitta	wildtype	0.005	0.005	19.564	0.799	0.434	-0.0003	0.0007
Right sagitta	mutant	0.006	0.005	16.603	1.934	0.070	-0.0006	0.002
Right sagitta	wildtype	0.005	0.005	15.959	0.236	0.816	-0.0005	0.0005

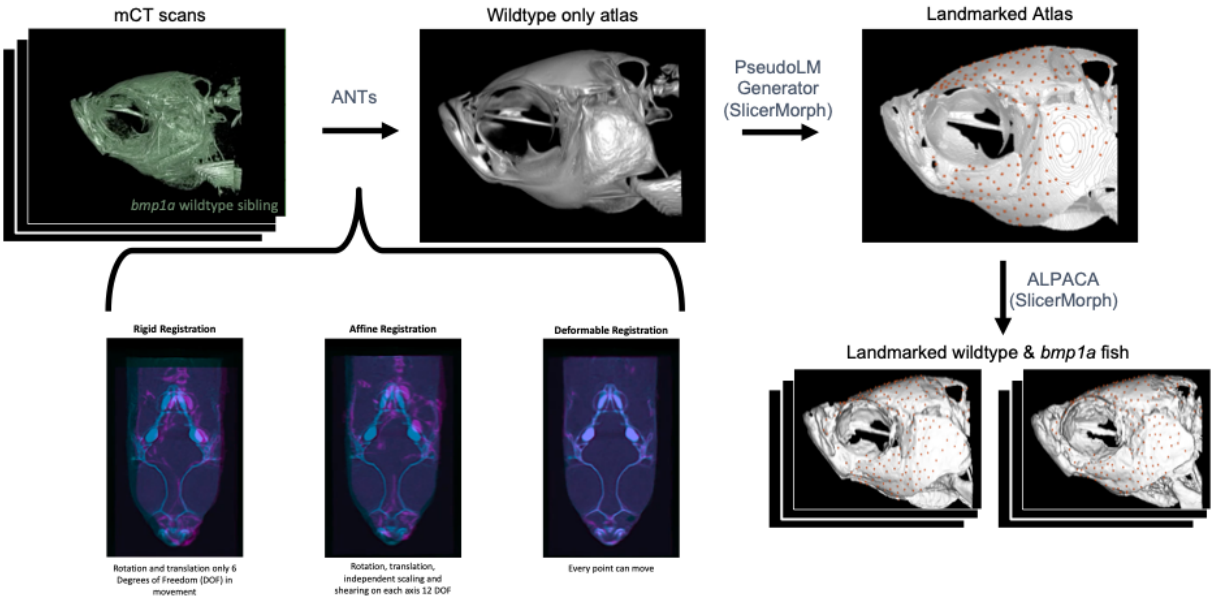

Figure 1. Pipeline for atlas building, pseudo-landmark generation, and transferring pseudo-landmarks to individual fish. Starting with microCT scans of wildtype fish ANTs, uses a series of rigid, affine, and deformable registrations to create an average image, or Atlas. The PseudoLMGenerator tool in SlicerMorph was used to place 372 pseudo-landmarks on the atlas. The ALPACA tool in SlicerMorph was used to transfer points from the atlas to wildtype and bmp1a fish for comparisons between groups.

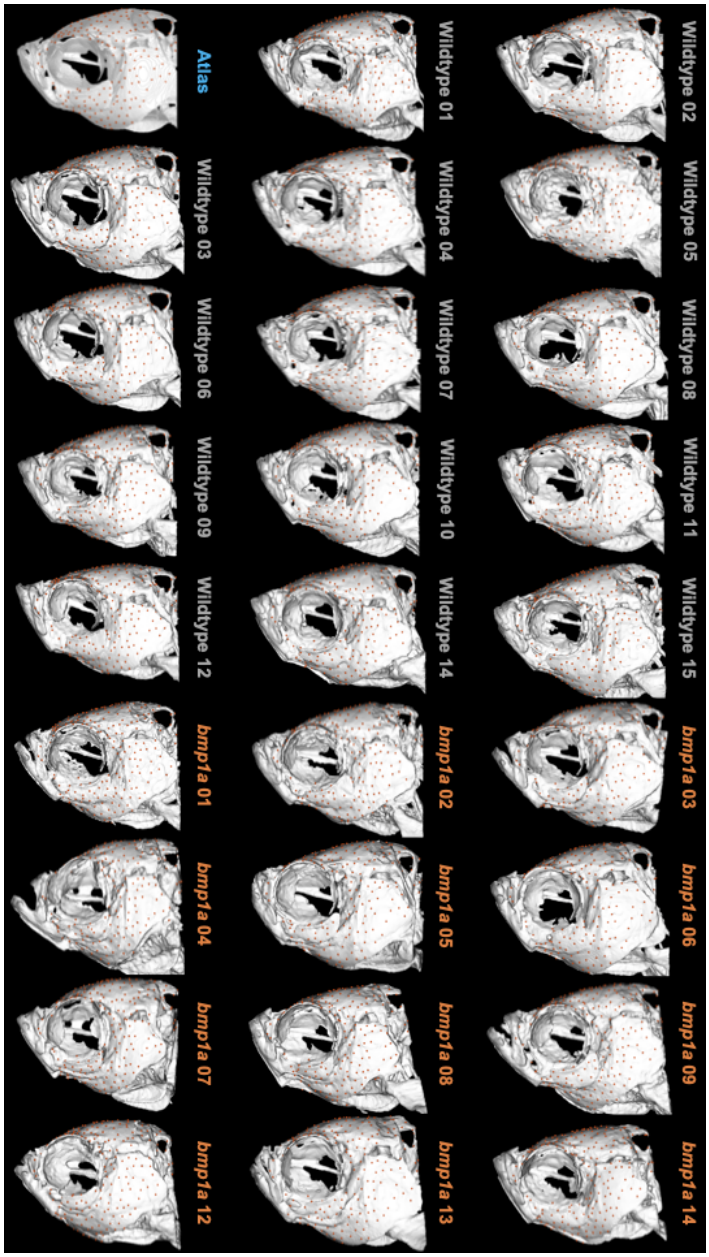

Figure 2. Left lateral view of fish meshes with pseudo-landmarks generated from the PseudoLMGenerator and transverse using the ALPACA modules in SlicerMorph. Name color represents groupings, the atlas is in blue, wildtype fish are in grey and *bmp1a* fish are in orange.

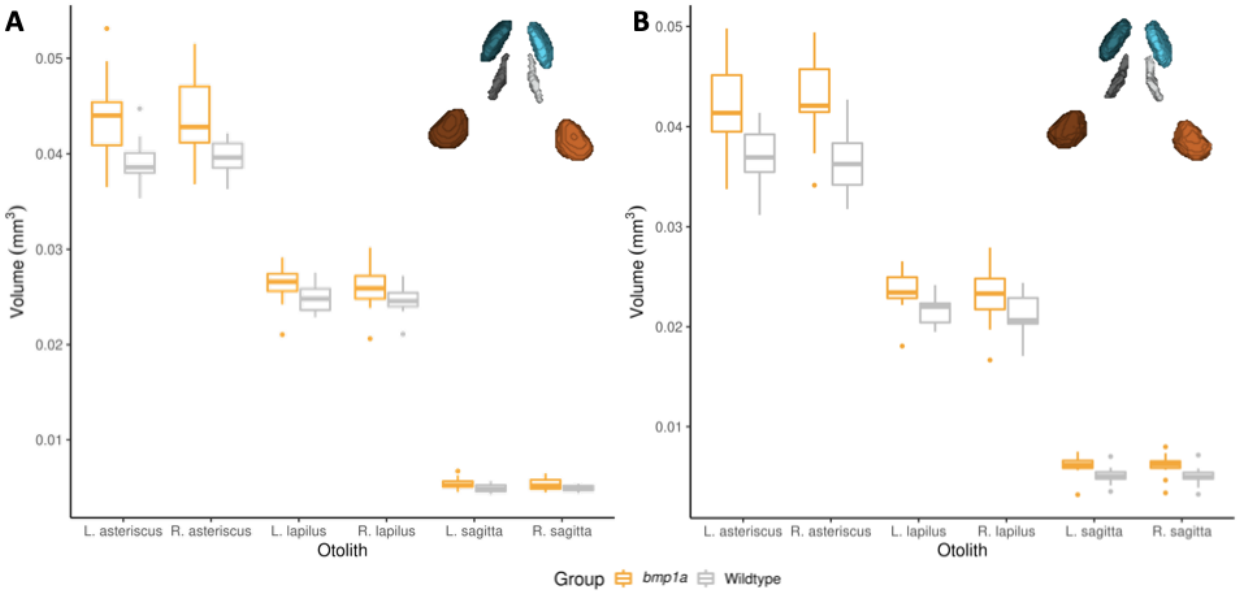

298

299 **Figure 3.** Boxplots of segmented otolith volumes. Wildtype (grey) and *bmp1a* mutant (orange)

300 boxplots are shown for each of the six otoliths for both the (A) manually segmented volumes

301 and (B) atlas segmented volumes. For each otolith, mutants have larger median volumes than

302 wildtype fish (Table 1). Insets show the dorsal view of otolith segments (asterisk in blue, lapilus

303 in orange, and sagitta in grey) with lighter colors on the left side of the head, and darker colors

304 on the right.

305

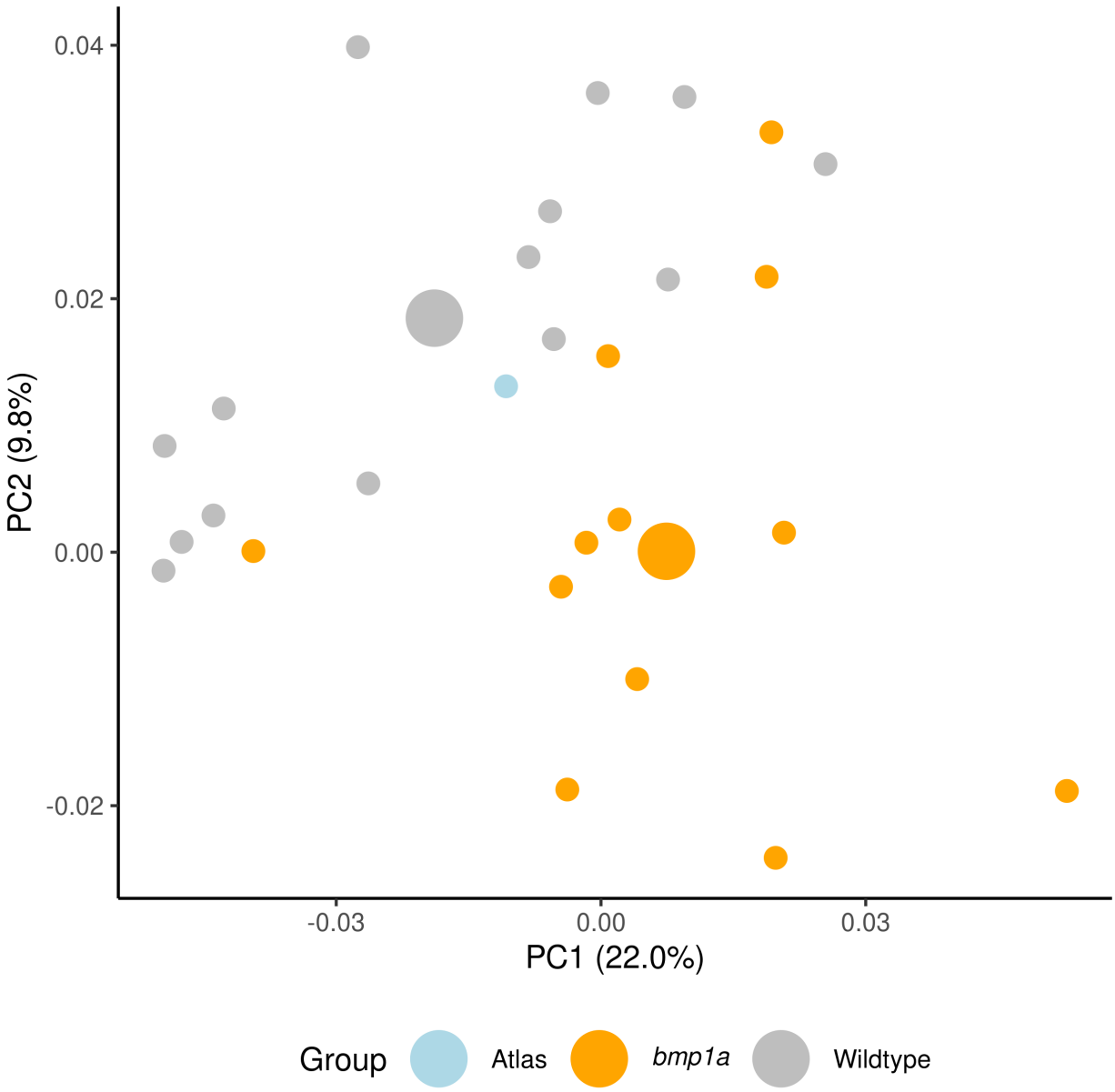

Figure 4. First two principal components from Generalized Procrustes Analysis. Color shows *bmp1a* (orange) or wildtype (grey) fish as well as the location of the atlas (blue) in morphospace. Larger circles show average position for each group. *bmp1a* and wildtype fish separate along both axes.

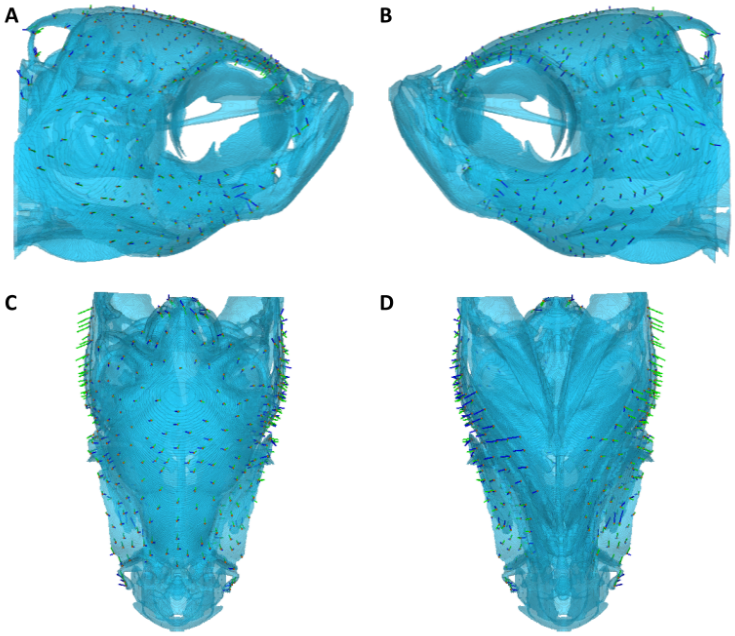

Figure 5. Landmark vector plots for first two principal components from GPA analysis. Vectors show magnitude and direction of variation along PC1(green) and PC2 (dark blue). Panels show (A) left lateral, (B) right lateral, (C) dorsal, and (D) ventral orientation of the zebrafish crania. Click here for animation.